# Electronic, dielectric, and optical properties of individual composite silver halide microcrystals using the EELS and LMTO-ASA techniques

Vladimir Oleshko*
*Department of Materials Science & Engineering, 116 Engineer's Way, University of Virginia, Charlottesville, Virginia 22904-4745*

Marc Amkreutz and Harald Overhof
*Theoretische Physik, Universität Paderborn, Warburger Strasse 100, 33098 Paderborn, Germany*
(Received 11 November 2002; published 17 March 2003)

The low-loss fine structure in electron energy-loss spectra (EELS) of individual composite high-aspect-ratio tabular Ag$X$($X$=Br, I) microcrystals between 4 and 26 eV was investigated by cryo-EELS and energy-filtering transmission electron microscopy. Local dielectric permittivity, refractive index, and absorption coefficient have been determined using Kramers-Kronig relationships. Quantum-mechanical calculations of the AgBr band structure and dielectric permittivity by the linear muffin-tin orbital method in the atomic spheres approximation have been used to assign the structure attributed to exciton peaks. Experimental local dielectric parameters and joint optical density of states were found to be in fair general agreement with calculated dielectric properties and densities of states.

DOI: 10.1103/PhysRevB.67.115409 PACS number(s): 71.15.Ap, 42.70.Gi, 71.20.−b, 71.15.Dx

## I. INTRODUCTION

Although the replacement of Ag$X$-based ($X$=Br, I) imaging systems by electronic imaging has been predicted two decades ago, their current world manufacturing level is larger than ever. However, in order to be eligible for incorporation into digital and hybrid information technologies for the 21st century, photographic materials must be further improved with respect to their quantum efficiency and image quality. In order to achieve these objectives, the key components should be intentionally modified with a focus primarily at the nanostructural level. By the introduction of high-aspect-ratio tabular Ag$X$ ($X$=Cl, Br, I) grains of mixed composition, by incorporation of phase boundaries in Ag$X$ microcrystals (doublestructured or multistructured composite crystals), and the controlled chemical and spectral sensitizations, the overall efficiency of the photographic process has been remarkably increased due to enhanced efficiency of quantum detection and reduced light scattering. Furthermore, the working grain volume has been decreased by a factor of 10 during the last decade. Granularity and speed of photographic materials employing advanced tabular grain technology can be modified over a wide range by a variation of development conditions, thus offering a better quality-to-speed ratio at middle and high densities.[1] An increased interest in the structural and analytical characterization of individual microcrystals and their compositional arrangement by various instrumental methods has been stimulated by the introduction of novel types of photographic emulsions with improved efficiency of light quanta detection, photohole trapping, and storage of the latent image.[2–9]

Fundamental research in this field is still in progress, since the silver halides exhibit many interesting physical and chemical properties. Among them, there are unusually small lattice constants, but large lattice energies and dielectric constants, peculiarities of elastic constants and phonon spectra, low solubility, predominance of Frenkel defects, high mobility of interstitials and dislocations, and remarkable quantum-size effects that have made them attractive for solid-state physics and chemistry.[10–14] In addition to the unique character of optical absorption, the Ag 4$d$ states and the halogen $p$ states in AgX are close to each other, thus leading to considerable complexity in the valence-band structure, as was confirmed by numerous reports.[15–20]

Due to their spatially resolved nature, energy-filtering transmission electron microscopy (EFTEM [equivalent to electron spectroscopic imaging (ESI)]), and electron energy-loss spectroscopy (EELS), may give an important new insight into the crystalline and electron structures of Ag$X$.[2] Higher spectral resolution of modern EELS (0.1–1.5 eV) as compared to conventional energy-dispersive x-ray spectroscopy (EDX, 130–150 eV) offers an opportunity to probe local electron excitations in the crystals. The limitations induced by the methods arise from the insulating properties and damage of Ag$X$ under the electron irradiation, which could be significantly reduced by cooling to liquid-nitrogen temperature.[2,3]

On the other hand, during the last two decades one of the most popular quantum-mechanical electron structure calculation techniques, the *ab initio* linear muffin-tin orbital method (LMTO),[21] in its atomic spheres approximation (ASA) has been extended to calculate the excited states and optical and other physical properties of materials from first principles.[22,23] Moreover, recent successful evaluation of spatial distribution of the conduction-band particle density in Ag$X$ with the LMTO-ASA treating exchange and correlation effects in the local spin-density approximation of the density-functional theory (LSDA-DFT) showed that the lowest conduction-band states contain essential contributions both from the halogen and from the large interstitial lattice regions.[24] This further shows the original LMTO-ASA technique by Andersen to be capable of calculating the optical properties of materials. In this paper we report the local electronic, dielectric, and optical properties of composite tabular Ag$X$ microcrystals studied by cryo-EELS/EFTEM and LMTO-ASA techniques.

 

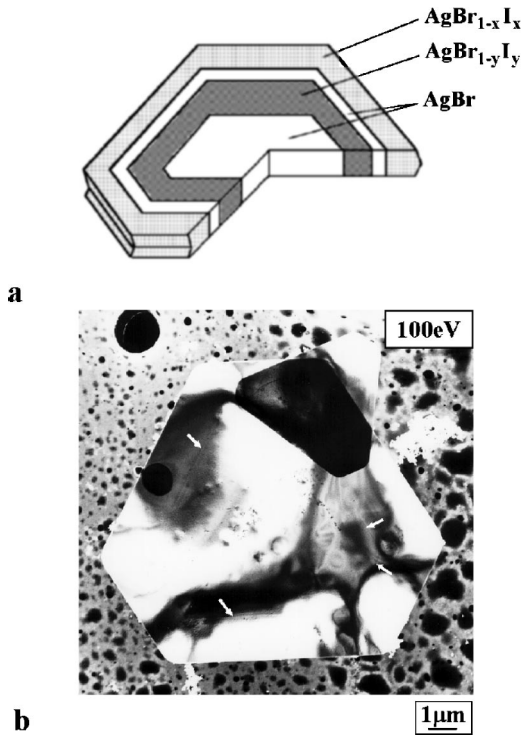


FIG. 1. Schematic view of a composite tabular microcrystal (a) containing an AgBr core ($100\pm20$nm thickness) and two Ag(Br, I) shells ($110\pm20$nm thickness), iodide atomic fractions in the corresponding shells are denoted as $x$ and $y$ ($x\approx0.03$, $y\approx0.08$) and cryo-EFTEM image of the composite tabular microcrystals (b) at $100\pm5$ eV energy losses near the [111] zone, $T=80$ K. Arrows point to stacking faults in the shell.

## II. EXPERIMENT

AgBr (core)–Ag (Br, I) (shell) composite tabular microcrystals, 2–10 $\mu$m in size [see Figs. 1(a) and 1(b)] containing 3–8 mol % of AgI in the shells were synthesized by a computer-assisted double jet method. Procedures of specimen preparation for microscopic studies have been described elsewhere.[3] All preparations and handling were done under nonactinic light to avoid the formation of printout silver. Measurements have been performed at an acceleration voltage of 80 kV using an analytical unit composed from a ZEISS CEM902 computerized electron microscope with an integrated energy filter (ESI/EELS) and a JEOL JEM1200EX TEMSCAN (STEM/EDX), both connected to a Kontron IBAS-2000 image analysis system.

EEL spectra were recorded by a photomultiplier serial detector interfaced to a PC/AT for automatic data acquisition. The illumination semiangle $\alpha$ was 2.5 mrad and the collection semiangle $\beta$ was varied from 6 to 35 mrad. The estimated energy resolution was 1.5 eV, based on the measured full width at half maximum of the zero-loss peak. The background was fitted according to the power-law function $AE^{-r}$ to reveal the positions of edges followed by smoothing using Savitsky-Golay filters to remove noise from the spectrum profiles. The KRAKRO program[25] with single scattering distributions applied as an input and the EELSKKT program[26] employing for this purpose recorded EEL spectra have been used to calculate the imaginary part $\mathrm{Im}(-1/\epsilon)$ of the energy-loss function and the real part $\epsilon_1$ and imaginary part $\epsilon_2$ of the relative dielectric permittivity as well. Radiation damage of Ag$X$ particles during measurements was reduced using a top-entry cryostage at $T=80$ K supplied with a modified evacuated cooling trap.

A JEOL1200EX TEMSCAN electron microscope was equipped with an EM-ASID10 scanning device and multidetector system and a NORAN TN5500 EDX analyzer; it was applied to carry out x-ray mapping and spot analysis in the bright- or dark-field scanning transmission electron mciroscopy mode. To minimize crystal damage under electron bombardment, the temperature of the specimen was kept at $T\leqslant95$ K by using a GATAN 636 double tilt-cooling holder.

## III. THEORETICAL APPROACH

The calculations have been performed using the *ab initio* linear muffin-tin orbital method in the atomic spheres approximation with the LSDA-DFT ansatz for the exchange and correlation effects.[21] Based on this formalism, expressions for the real and imaginary parts of the dielectric permittivity have been derived using a simplified model. Taking into account only direct transitions, which conserve the $k$ vector, one obtains for the imaginary part:

$$\epsilon_2=\frac{2\hbar^2e^2}{\pi m^2\omega^2}\sum_{jj'}\int_{\mathrm{BZ}}|M_{jj'}(\vec{k})|^2\delta(E_{j'}(\vec{k})-E_j(\vec{k})-\hbar\omega)d^3k. \tag{1}$$

Here $M_{jj'}$ are the transition-matrix elements for transitions from band number $j$ to $j'$ with $\vec{k}=\vec{k}_j=\vec{k}_{j'}$ and $m$ is the electron mass. Since real and imaginary parts are interconnected by the Kramers-Kronig relations, the expression for $\epsilon_1$ reads

$$\epsilon_1=1+\frac{2\hbar^4e^2}{\pi^2m^2}$$

$$\times\sum_{jj'}P\int_{\mathrm{BZ}}\frac{|M_{jj'}(\vec{k})|^2}{[E_{j'}(\vec{k})-E_j(\vec{k})]^2[E_{j'}(\vec{k})-E_j(\vec{k})-\hbar\omega]}d^3k. \tag{2}$$

Here $P$ denotes the principal value of the integral. Assuming all transition-matrix elements to be independent of the $k$ point and the band number of the initial and final electron state, Eq. (1) is simplified to

$$\epsilon_2=\frac{V_2}{\omega^2}\sum_{jj'}\int_{\mathrm{BZ}}\delta(E_{j'}(\vec{k})-E_j(\vec{k})-\hbar\omega)d^3k \tag{3}$$

with

$$V_2=\frac{2\hbar^2e^2}{\pi m^2}|M|^2, \tag{4}$$

while Eq. (2) transforms to

$$\epsilon_1 = 1 + V_1 \times \sum_{jj'} P \int_{\mathrm{BZ}} \frac{1}{[E_{j'}(\vec{k}) - E_j(\vec{k})]^2 [E_{j'}(\vec{k}) - E_j(\vec{k}) - \hbar\omega]} d^3k \tag{5}$$

with

$$V_1 = \frac{2\hbar^4 e^2}{\pi^2 m^2} |M|^2. \tag{6}$$

Within this approximation of constant transition-matrix elements, real and imaginary parts of the dielectric permittivity are calculated from the energies provided by the self-consistent LMTO-ASA energy band calculations.

## IV. RESULTS AND DISCUSSION

Multistructured composite tabular microcrystals 2–10 $\mu$m in size and 100–120 nm in thickness used in the study consist of an AgBr core surrounded by two shells enriched with iodide, $AgBr_{0.97}I_{0.03}$ and $AgBr_{0.92}I_{0.08}$, respectively, as schematically shown in Fig. 1(a). Figure 1(b) presents an energy-filtered micrograph of the tabular grains taken at 100-eV energy losses with a 10-eV energy window. Observations of the crystals using energy filtering in the range 0–100 eV indicate that the Bragg contrast is preserved not only under zero losses, when the blurring and chromatic aberrations caused by inelastically scattered electrons are avoided, but also in inelastic scattering processes exciting plasmons and excitons superimposed with low-intensity inner-shell ionization edges.[27] Furthermore, as one can see from Fig. 1(b), blurring of edge contours by a spectrum of excitation errors due to the angular distribution of inelastically scattered electrons is still insignificant at 100-eV energy losses. The image exhibits the unusual ''negative'' contrast because of variations of the electron intensity, while intersecting a tail of the intensive bulk plasmon, followed by a decrease in the background intensity with increasing energy losses. This leads to the observed contrast reversal, when the selected energy is tuned over the range of 0–100 eV.

The shape of the microcrystals that approximates either a regular hexagon or a truncated triangle is assigned to the lateral growth along the side $\{11\bar{1}\}$ planes originated by multiple twin planes parallel to the (111) surface. Because of high aspect ratio ($\sim 20-100$) and relatively large specific area, tabular microcrystals may significantly enhance quantum efficiency and reduce light scattering. They also allow reduced silver deposition and thinner photographic layers as compared to conventional isometric (cubic, octahedral, and mixed shapes) Ag*X* emulsion grains. Lattice distortions due to a few percent of iodide incorporated in the shells result in atom displacements perpendicular to the core-shell interface. In turn, this decreases the cationic sublattice binding energy, initiating various types of surface and internal defects (stacking faults, dislocations, and Frenkel point defects), clustering of iodine at nucleation points, and long period surface ordering of iodide ions.[4] So, the optimum contrast improved by tuning allowed to observe narrow black lines in the shell region pointed by arrows, which indicate the presence of $\{11\bar{1}\}$ stacking faults parallel to $\{11\bar{2}\}$ grain edges. The composite structural arrangement of the grains with the AgBr core and iodide concentrations in the shells increasing from the center to the edges, as expected,[28,29] should promote preferential migration of photoelectrons to the AgBr core and photoholes in opposite direction, thus resulting in concentrating latent image centers within the core. Trapping of mobile holes on defective phase boundaries should additionally stimulate a better separation of photoelectrons and holes during the formation of latent image.

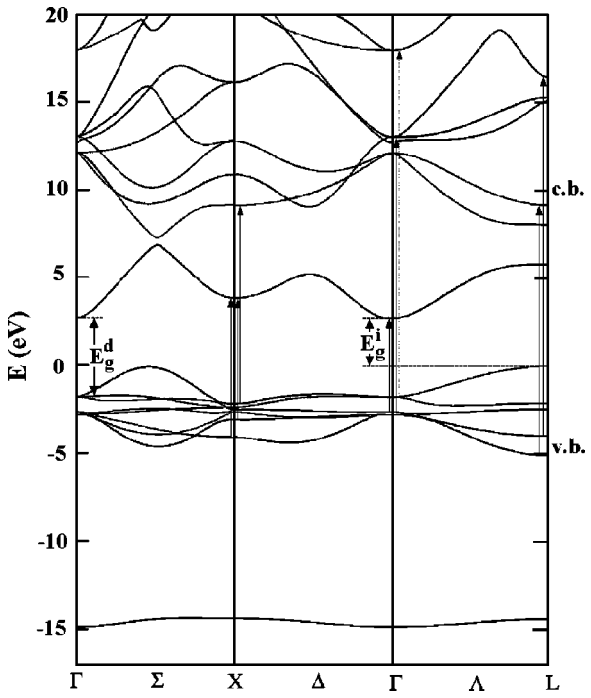


FIG. 2. Electronic band structure of AgBr calculated by the *ab initio* LMTO-ASA method with a proposed assignment of experimentally observed exciton assisted interband transitions at Γ, *L*, and *X*. $E_g^d$ and $E_g^i$ denote energies of the lowest direct and indirect gap, respectively, v.b. is the valence band, c.b. is the conduction band.

From the Korringa-Kohn-Rostoker computations of band structure for AgBr (Refs. 30 and 31) and later calculations by the LMTO-ASA technique (Fig. 2), the lowest conduction band is *s*-like and isotropic with the minimum at $\Gamma_6^+$. The gap between first and second conduction bands is artificial due to the intercept point lying beyond the considered main symmetry axis (compare, e.g., Vogel *et al.*[15]).

In contrast, the valence-band structure is more complex, which reflects a considerable degree of covalency. There is no mixing of the states at $\Gamma(\vec{k}=0)$ because of the inversion symmetry. The uppermost maximum at *L* due to strong mixing for $\vec{k} \neq 0$ and repelling the valence-band states gives rise to the indirect character of interband transitions. Spin-orbit interaction results in a split of $\Gamma_{15}$ into $\Gamma_6^-$ and $\Gamma_8^-$ and of $L_3$ into $L_6^-$ and the degenerated $L_4^-$, $L_5^-$ bands, respectively. Observed interband transitions are marked in Fig. 2.

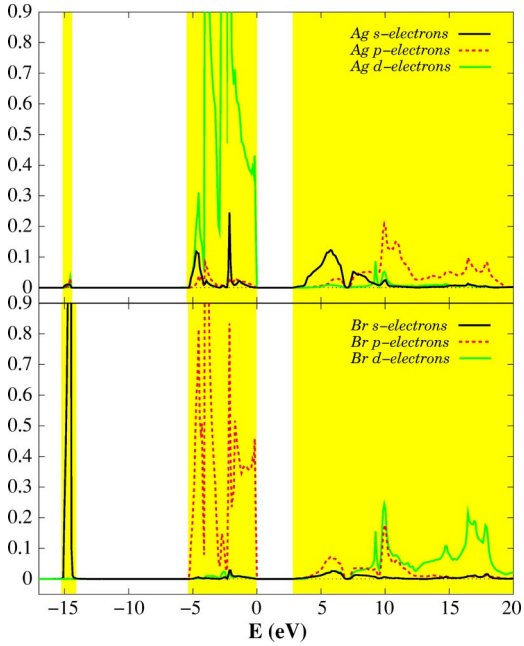


FIG. 3. Projected density of states (DOS) calculated within the LMTO-ASA approach, splitted into *s*-, *p*-, and *d*-orbital momentums of the Ag and Br atoms.

Figure 3 presents an overview plot of the projected density of states (DOS) splitted into *s*-, *p*,- and *d*-orbital momentums of the projected Ag and Br atoms. One can see the Br *s*-state at -15 eV and the Br *p*-states and Ag *d*-states mixing between $-5$ and 0 eV. This proximity of Ag $4d$ and Br $4p$ states lying within about 1 eV to each other is the reason for the strong covalent character of AgBr. Strong mixing of the Ag *s*, *p*, and valence *d* states and the Br valence *p* and *d* states occurs above the Fermi level. The first conduction band at 3–7 eV seems to be mainly a mixture of the Ag *s* states and the Br *p* states, while the second and the third ones are due to complicated mixing of the Br *d* and *p* states with the Ag *p* and *d* states.

The single scattering EEL intensity expressed as the differential cross section $d^2\sigma/d\Omega dE$ is related to the imaginary part of the reciprocal complex dielectric permittivity $\epsilon(\vec{q},E)$ as a function of wave vector $\vec{q}$ and energy $E$. It thus reflects the local dielectric response of the media to a longitudinal field:[32]

$$\frac{d^2\sigma}{d\Omega dE} \propto \mathrm{Im}\left(-\frac{1}{\epsilon(\vec{q},E)}\right)\ln\left(1+\frac{\beta^2}{\Theta_E^2}\right), \tag{7}$$

where $\beta$ is the collection semiangle (the illumination semiangle $\alpha<\beta<\sqrt{E/E_0}$), $\Theta_E=E/2T\sqrt{1-v^2/c^2}$ is the characteristic scattering angle; $T=1/2mv^2=E_0(1+E_0/2mc^2)/(1+E_0/2mc^2)^2$; $m$ is the free electron mass; $v$ is the velocity of the incident electrons; $c$ is the velocity of light, and $E_0$ is the initial energy of the incident electrons. Figure 4 shows the real and imaginary parts of the dielectric permittivity, $\epsilon(\vec{q},E)=\epsilon_1(\vec{q},E)+i\,\epsilon_2(\vec{q},E)$, and the energy-loss function computed using Kramers-Kronig relations for the AgBr core of a tabular microcrystal.[3] The curves $\epsilon_2$ and $\mathrm{Im}(-1/\epsilon)$ fall

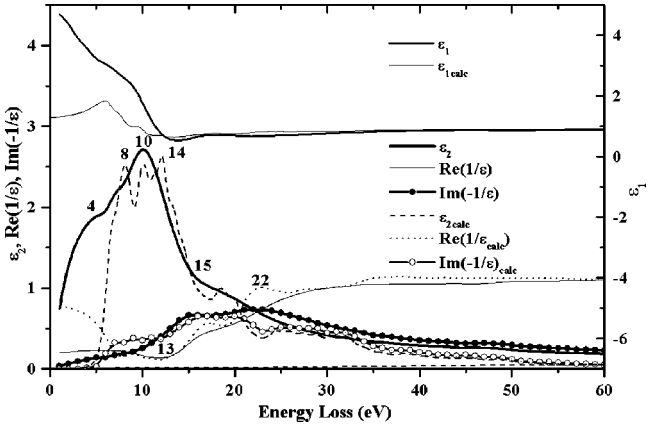


FIG. 4. Dielectric permittivity and energy-loss function for an AgBr core of a composite tabular microcrystal versus. self-consistent LMTO-ASA calculations.

to 0 at $E\leqslant 3$ eV, reflecting the position of the indirect exciton band gap $E_g^i$ at 2.68 eV.[30,31] The real part $\epsilon_1(\vec{q},E)$ describes the polarizability of the specimen, while the imaginary part $\epsilon_2(\vec{q},E)$ is related to absorption in the specimen. The energy-loss function is expressed as

$$\mathrm{Im}\left(-\frac{1}{\epsilon(\vec{q},E)}\right)=\frac{\epsilon_2}{\epsilon_1^2+\epsilon_2^2}=\frac{\omega\Gamma\omega_p^2}{(\omega^2-\omega_p^2)^2+(\omega\Gamma)^2}, \tag{8}$$

where $\Gamma$ is the damping constant, and $\omega_p$ is the plasma resonance frequency. The energy of the volume plasma resonance, $\hbar\omega_p$, for the particular excitonic system was estimated in a first approximation as[33]

$$\hbar\omega_p=\sqrt{(\hbar\omega_p^f)^2+(E_g^i)^2}=\sqrt{21.4^2+2.7^2}\ \text{eV}\approx 21.6\ \text{eV}. \tag{9}$$

Here $\hbar\omega_p^f=\sqrt{ne^2/(\epsilon_0 m_0)}=2.14$ eV is the free electron plasma energy with $\hbar\omega_p^f$ being the corresponding frequency, $n$ is the AgBr electron density, $e$ the electron charge, $\epsilon_0$ the permittivity of vacuum, and $m$ the electron mass. The energy of the free electron plasma was calculated assuming 16 valence outer-shell electrons [$4d$ ($Ag^+$, ten electrons) and $4p$ ($Br^-$, six electrons)] as free. The estimated energy of the volume plasmon appeared to be close to the experimental value within the accuracy of measurements. The free electron plasma frequency is $\omega_p^f=3.3\times10^{16}$ Hz.

The low-loss EEL spectra of tabular Ag$X$ ($X$=Br, I) microcrystals are dominated by collective outer-shell excitations (excitons and plasmons superimposed with interband transitions and excitations from defect levels into unoccupied states.[3,27] For low energy losses $E\leqslant\hbar\omega_p\approx 21.6$ eV, the energy-loss function describes collective electron excitations against an ionic background caused by oscillations of bound electrons (interband transitions). When $\epsilon_1$ is zero or has a local minimum (which points to instability of the electron system against small external perturbations, leading to excitations) and $\epsilon_2$ is still small enough (indicating small damping of oscillations due to absorption), the function

$\mathrm{Im}(-1/\epsilon(\vec{q},E))$ exhibits maxima corresponding to oscillations at 4, 7–8, 15–17, and 22–24 eV.

In line with studies of uv absorption and reflectivity on AgBr,[34,35] the feature at 4 eV in $\epsilon_2$ was attributed to unresolved direct exciton transitions involving the spin-orbit split valence and conduction-band states at the $\Gamma$ point, i.e. ($\Gamma_8^-$, $\Gamma_6^- \rightarrow \Gamma_6^+$, see Fig. 2). The shoulder at about 8 eV and intense peak at 10 eV were assigned to exciton transitions at the $X$ point [unresolved ($X_6^-$, $X_6^-$, $X_7^- \rightarrow X_6^+$].[35] The band at 15–17 eV was assigned to higher-energy exciton transitions, particularly with $\Gamma_6^+$ symmetry. Although $\mathrm{Im}(-1/\epsilon(\vec{q},E))$ revealed the essential similarity for samples under study, $\epsilon_1$ and $\epsilon_2$ exhibited some differences.

LMTO-ASA calculations of the real and imaginary parts of the dielectric permittivity and of the energy-loss function of crystalline AgBr have been performed using the described approach with fitting parameters $V_1=1/25$ and $V_2=1/95$. For comparison with the experimental data the computed functions have been smoothed by use of a Gaussian with a width of $E_0=0.025$ eV. These smoothed LMTO-ASA calculations compared with the experimental data for AgBr are also shown in Fig. 4.

Although $\epsilon_{2\,\mathrm{calc}}$ and $\mathrm{Im}(-1/\epsilon_{\mathrm{calc}})$ fall to zero at 4.3 eV (the direct band gap of AgBr) due to limitations of the model, the maxima of $\epsilon_2$ at 9 eV, 11 eV, and 13 eV satisfactorily fit to the intensive composite band at 7–14 eV (with maxima at 8 eV and 10 eV). The assignment of the peak at 10 eV to the proposed exciton transitions at the $X$ point is supported by the calculations, which show a minimum at 10 eV in $\epsilon_{2\,\mathrm{calc}}$. However, the main contribution to this peak is supposed to refer to direct band-to-band transitions, from the valence bands between $-5$ eV to $-3$ eV to the lowest conduction band at 4–7 eV and from the top valence band at $-2$ to 0 eV to the conduction band at 10 eV.

The minimum of computed $\epsilon_1$ at 14 eV fits well to the minimum of the experimental $\epsilon_1$ curve, similarly to the minimum of Re $(1/\epsilon)$ at 13 eV. Afterwards, both $\epsilon_1$ and $\mathrm{Re}(1/\epsilon)$ converge towards 1. The agreement between experimental and calculated $\epsilon_1$ is reasonable except for the lower frequencies, where the neglect of excitonic effects in the theoretical approach gives rise to major discrepancies. The same holds for $\mathrm{Re}(1/\epsilon)$, where the agreement is satisfying down to 7 eV.

The crossings of $\mathrm{Re}(1/\epsilon)$ and $\mathrm{Im}(-1/\epsilon)$ at 8 eV where $\epsilon_1=\epsilon_2$ coincide as well as of $\mathrm{Re}(1/\epsilon)$ and $\epsilon_2$ at 22 eV, where $\mathrm{Im}(-1/\epsilon)$ has its maximum and $\epsilon_1$ has a local minimum. Furthermore, there is the shoulder of $\epsilon_2$ at 15–16 eV superimposed with the previous band and the corresponding maximum of $\mathrm{Im}(-1/\epsilon)$. For $E>25$ eV, both computed and experimental curves are very close. Again, the features at 4–5 eV cannot be computed due to having no direct transitions at this energy, but except that, especially the calculated absorption $\epsilon_{2\,\mathrm{calc}}$ and therefore the energy-loss function $\mathrm{Im}(-1/\epsilon)$ accord well with the experimental data. So, this simple model based on the LMTO-ASA method seems capable of describing the qualitative behavior of the dielectric permittivity properly and giving hints of exciton transition regions. It is also evident that within the LMTO-ASA formalism not only the valence-band structure is well characterized, but also the conduction-band structure, and that the computed functions $\epsilon_1$ and $\epsilon_2$ essentially reflect the band structure and density of states of AgBr.

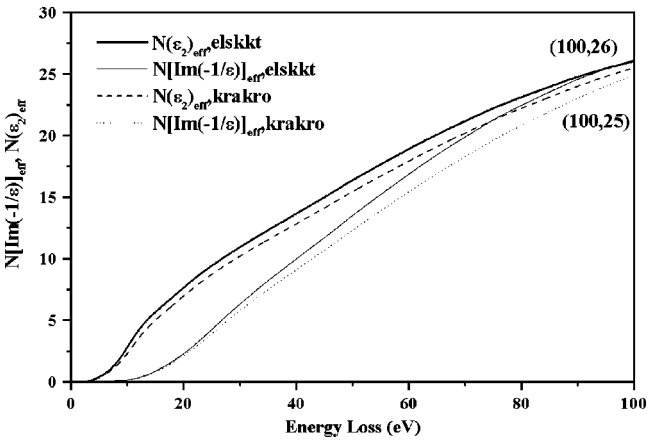


FIG. 5. Effective number of electrons per atom, $N$, contributing up to 100-eV energy losses.

As a check on the data based on the Bethe sum rule, an effective number of electrons per AgBr unit contributing up to 100-eV energy losses, $N_{\mathrm{eff}}$, was calculated (Fig. 5) using the following equations:[25]

$$N_{\mathrm{eff}}(\epsilon_2)=\frac{2\epsilon_0 m_0}{\pi\hbar^2 e^2 n_{\mathrm{AgBr}}}\int_0^E E'\,\epsilon_2(E')dE', \tag{10}$$

$$N_{\mathrm{eff}}(\mathrm{Im}(-1/\epsilon))=\frac{2\epsilon_0 m_0}{\pi\hbar^2 e^2 n_{\mathrm{AgBr}}}\int_0^E E'\,\mathrm{Im}(-1/\epsilon(E'))dE', \tag{11}$$

where $n_{\mathrm{AgBr}}=20.8\ \mathrm{nm}^{-3}$ is the number of AgBr units per unit volume. The effective numbers of electrons $N_{\mathrm{eff}}(\epsilon_2)$ and $N_{\mathrm{eff}}(\mathrm{Im}(-1/\epsilon))$ converge towards 25–26, although $N_{\mathrm{eff}}(\mathrm{Im}(-1/\epsilon))$ remains reasonably less than $N_{\mathrm{eff}}(\epsilon_2)$ at low energy losses. This is due to the $1/E$ weighting factor in the relationship between a double-differential cross section and generalized oscillator strength per unit energy loss.[25] In the limit of $E\rightarrow\infty$ (practically at 150–160 eV) the total number of valence electrons per formula unit reaches 34 $=16\ (4p^6 4d^{10},\ \mathrm{Ag}^+)+18\ (3d^{10}4s^2 4p^6,\ \mathrm{Br}^-)$. The difference up to 100-eV energy losses can be assigned to that eight or nine from ten $3d(\mathrm{Br}^-)$ and $4p\ (\mathrm{Ag}^+)$ electrons practically do not contribute in the selected range because related inner-shell excitations, Ag $N_{2,3}$ at 59 eV and Br $M_{4,5}$ at 70 eV, are delayed and occur before the valence-electron contribution is exhausted.

In Fig. 6(a) the real part (index of refraction),

$$n=\sqrt{\frac{1}{2}\left(\sqrt{\epsilon_1^2+\epsilon_2^2}+\epsilon_1\right)}, \tag{12}$$

and the imaginary part (extinction coefficient),

$$k=\sqrt{\frac{1}{2}\left(\sqrt{\epsilon_1^2+\epsilon_2^2}-\epsilon_1\right)} \tag{13}$$

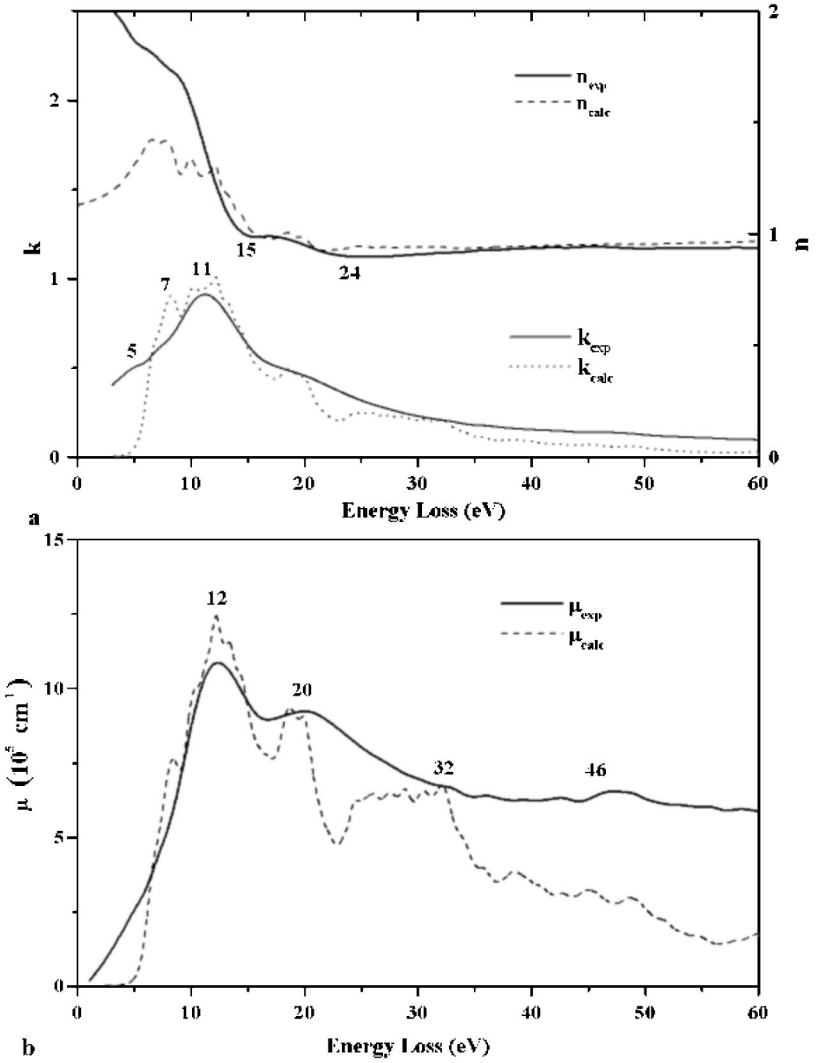


FIG. 6. Local complex refractive index $N=n+ik$ (a) and absorption coefficient $\mu(E)$ (b) of an individual tabular microcrystal, an AgBr core, and corresponding computed quantities.

of the local complex refractive index, $N=\epsilon^{1/2}=n+ik$, of an individual composite tabular microcrystal, calculated from EELS data acquired within areas of about 100 nm in size for the AgBr core, and the computed $n$ and $k$ are given. One can easily notice that the values of $n$ closely approach 1.0 above 50 eV. Again, we found a good agreement of the experimental and calculated curves, especially for the minima at 15 and 24 eV of $n$ and the shoulder at 7 eV and the maximum at 11 eV of $k$. The extinction coefficient $k$ is directly related to $\epsilon_2$ with $k=\epsilon_2/(2n)$, and because of $n$ being almost 1 from 16 eV on, the behavior of $k$ is trivial. The local absorption coefficient,

$$\mu(E)=\frac{E}{\hbar c}\sqrt{2(\sqrt{\epsilon_1^2+\epsilon_2^2}-\epsilon_1)}=\frac{2E}{\hbar c}k \qquad (14)$$

calculated using the same EEL spectra for the crystal AgBr core, is shown in Fig. 6(b). In spite of the limited resolution of the used EEL spectrometer, the values of $\mu(E)$ satisfactorily agree with the earlier reported results of Carrera and Brown,[34] who measured the transmission of AgBr thin films in the near uv direct exciton region (3.5–6.7 eV) and above 30 eV using synchrotron radiation.

In addition, maxima of the real part of the optical joint density of states (OJDOS),

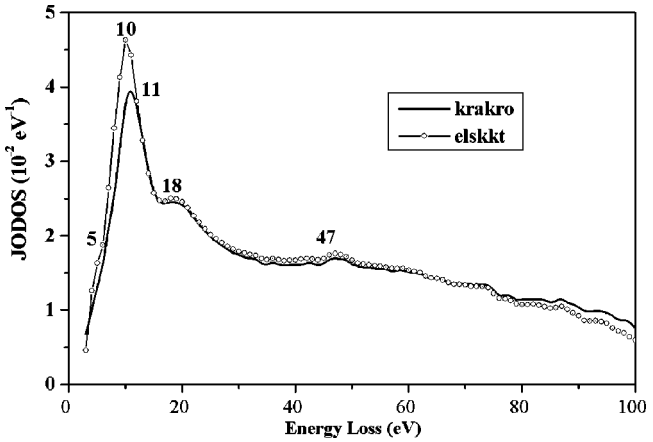


FIG. 7. Real part of optical joint density of states (OJDOS), $\mathrm{Re}(J_1(E))$ calculated from experimental data with the KRAKRO and ELSKKT programs, respectively.

$$\mathrm{Re}(J_1(E)) = \frac{E\,\epsilon_2}{0.5\,\pi E_p^2}, \tag{15}$$

with the energy of the free electron plasma $E_p = 21.4$ eV, at about 5 eV, 10–11 eV, and at 18 eV (Fig. 7) satisfactorily fit to the corresponding maxima of the calculated DOS in Fig. 3.

## V. CONCLUSION

The use of cryo-ESI/EELS combined with LMTO-ASA quantum-mechanical calculations provides us with useful insights into understanding of local electronic, dielectric, and optical properties of individual high-aspect-ratio composite [AgBr core–Ag(Br, I) shells] tabular microcrystals of contemporary photographic emulsion which are inaccessible by other techniques. For the AgBr core, experimental local dielectric permittivity, refractive index, absorption coefficient, and joint optical density of states determined via Kramers-Kronig analysis of the low-loss fine structure between 4 and 26 eV energy losses in EEL spectra of individual microcrystals were found to be in fair general agreement with corresponding calculated parameters. Ab initio quantum-mechanical calculations of the AgBr band structure and dielectric permittivity by the LMTO-ASA method in the LSDA-DFT approximation have been successfully used to assign the structure attributed to exciton peaks. We have demonstrated that the simple LMTO-ASA based model limited to only direct transitions above 4.3 eV is capable of describing properly the qualitative behavior of the dielectric permittivity and of giving hints on exciton transition regions. Moreover, it was found that within the LMTO-ASA formalism not only the valence-band structure is well characterized, but also the conduction-band structure, and that the real and imaginary parts of the dielectric permittivity essentially reflect the band structure and density of states of AgBr.

## ACKNOWLEDGMENTS

One of the authors (VPO) is thankful to Professor Dr. Renaat Gijbels and Professor Dr. Wim Jacob, University of Antwerp, Wilrijk, Belgium for support of this research and useful discussions.

*Email address: vpo6n@virginia. edu

[1] K. Topfer and R. Jacobson, J. Photogr. Sci. **41**, 25 (1993).
[2] V. Oleshko, in *Industrial Applications of Electron Microscopy*, edited by Z.R. Li (M. Dekker, New York, 2002), pp. 51–112.
[3] V. Oleshko, R. Gijbels, and W. Jacob, Micron **31**, 55 (2000).
[4] C. Goessens, D. Schryvers, and J.V. Landuyt, J. Microsc. Res. Tecn. **42**, 85 (1998).
[5] V. Oleshko, Microsc. Res. Tech. **42**, 82 (1998).
[6] A. Millan, P. Bennema, A. Verbeeck, and D. Bollen, J. Cryst. Growth **192**, 215 (1998).
[7] H. Saijo and M. Shiojiri, Microsc. Res. Tech. **42**, 123 (1998).
[8] G. Bögels, J. Buijnsters, S. Verhaegen, H. Meekes, P. Bennema, and D. Bollen, J. Cryst. Growth **203**, 554 (1999).
[9] G. Verlinden, R. Gijbels, and I. Geuens, Microsc. Microanal. **8**, 216 (2002).
[10] M. Bucher, Phys. Rev. B **30**, 947 (1984).
[11] J.F. Hamilton, Adv. Phys. **37**, 359 (1988).
[12] A.P. Marchetti, K.P. Johansson, and G.L. McLendon, Phys. Rev. B **47**, 4268 (1993).
[13] M. Freedhoff, A. Marchetti, and G. McLendon, J. Lumin. **70**, 400 (1996).
[14] A.P. Marchetti, P.J. Rodney, and W. von der Osten, Phys. Rev. B **64**, 132201 (2001).
[15] D. Vogel, P. Krüger, and J. Pollmann, Phys. Rev. B **58**, 3865 (1998).
[16] M. Mason, Phys. Rev. B **11**, 5094 (1975).
[17] J. Tejeda, N. Shevchik, W. Braun, A. Goldmann, and M. Cardona, Phys. Rev. B **12**, 1557 (1975).
[18] S. Ves, D. Glotzel, M. Cardona, and H. Overhof, Phys. Rev. B **24**, 3073 (1981).
[19] M.G. Mason, Y.T. Tan, T.J. Miller, G.N. Kwawer, F.C. Brown, and A.B. Kunz, Phys. Rev. B **42**, 2996 (1990).
[20] R.H. Victora, Phys. Rev. B **56**, 4417 (1997).
[21] O.K. Andersen, Phys. Rev. B **12**, 3060 (1975).
[22] U. Gerstmann, M. Amkreutz, and H. Overhof, Phys. Rev. B **60**, R8446 (1999).
[23] M. Alouani and J. Wills, in *Electronic Structure and Physical Properties of Solids: The Uses of the LMTO Method*, edited by H. Dreysse (Springer-Verlag, Berlin, 2000), pp. 168–187.
[24] H. Overhof and U. Gerstmann, Phys. Rev. B **62**, 12 585 (2000).
[25] R.F. Egerton, *Electron Energy-Loss Spectroscopy in the Electron Microscope*, 2nd ed. (Plenum, New York, 1996).
[26] A. Buxbaum, Master's thesis, Northwestern University, Evanston, Illinois, 1988.
[27] V. Oleshko, R. Gijbels, and W. Jacob, J. Microsc. **181**, 27 (1996).
[28] F. Granzer, J. Imaging Sci. **33**, 207 (1989).
[29] F. Granzer, J. Imaging Sci. **35**, 136 (1991).
[30] W. von der Osten, in *Polarons and Excitons in Polar Semiconductors and Ionic Crystals*, edited by J.T. Devreese and F. Peeters (Plenum, New York, 1982), pp. 293–342.
[31] H. Overhof, in *Numerical Data and Functional Relationships in Science and Technology*, edited by O. Madelung, Vol. 17, Pt. b (Springer, Heidelberg, 1982), Landolt-Börnstein, New Series, p. 515.
[32] R.F. Egerton, Ultramicroscopy **28**, 215 (1989).
[33] I. Egri, Solid State Commun. **44**, 563 (1982).
[34] N.J. Carrera and F.C. Brown, Phys. Rev. B **4**, 3651 (1971).
[35] W.F.F. Bassani and R.S. Knox, Phys. Rev. B **137**, A1217 (1965).